Published online 12 April 2010

Nucleic Acids Research, 2010, Vol. 38, No. 15 ***5105–5118***
doi:10.1093/nar/gkq210

Dynamics on multiple timescales in the RNA-directed RNA polymerase from the cystovirus ϕ6

Zhen Ren[1,2], Hsin Wang[1] and Ranajeet Ghose[1,2,*]

[1]Department of Chemistry, The City College of New York, New York, NY 10031 and [2]The Graduate Center of the City University of New York, New York, NY 10016, USA

Received February 4, 2010; Revised March 10, 2010; Accepted March 11, 2010

ABSTRACT

The *de novo* initiating RNA-directed RNA polymerase (RdRP), P2, forms the central machinery in the infection cycle of the bacteriophage ϕ6 by performing the dual tasks of replication and transcription of the double-stranded RNA genome in the host cell. By measurement and quantitative analysis of multiple-quantum spin-relaxation data for the δ1 positions of Ile residues that are distributed over the 3D-fold of P2, we find that the enzyme is dynamic both on the fast (ps–ns) and slow (μs–ms) timescales. The characteristics of several motional modes including those that coincide with the catalytic timescale (500–800/s) are altered in the presence of substrate analogs and single-stranded RNA templates. These studies reveal the plasticity of this finely tuned molecular machine and represent a first step towards linking structural information available from a host of crystal structures to catalytic mechanisms and timescales obtained from the measurements of kinetics for homologous systems in solution.

INTRODUCTION

RNA directed RNA polymerases (RdRPs) utilize RNA templates to catalyze the formation of a phosphodiester bond between nucleoside triphosphate (NTP) substrates. RdRPs are key in sustaining the growth, propagation and infection cycle of RNA viruses. The high-resolution structures of a variety of viral RdRPs reveal a conserved overall domain architecture shaped like a cupped hand containing 'fingers', 'thumb' and 'palm' domains (Supplementary Figure S1a) (1). RdRPs contain six conserved sequence motifs also found in DNA polymerases (A–E in the palm domain and F in the fingers domain) (2,3). These motifs that play a central role in catalyzing the nucleotidyl transfer reaction are responsible for binding metal ions, NTPs and RNA.

P2 (4), the 75-kDa RdRP from the cystovirus ϕ6 inititates the *de novo* synthesis of both minus-strand RNA (replication) (5) and plus-strand RNA (semi-conservative transcription) (6) and lies at the heart of the four protein polymerase complex central to the cystoviral life cycle (7,8). Multiple high-resolution crystal structures exist for P2 in the apo-form, and in complex with NTPs (and NTP-analogs), single-stranded DNA (ssDNA) and single-stranded RNA (ssRNA) templates (9–11). While these structures of P2 and indeed of several other RdRPs (1) provide atomic snapshots along the catalytic pathway, extensive flexibility both at the domain level and at the level of local motifs seems essential to reconcile biochemical data with structural information (12). For example, in P2 and in the homologous hepatitis C virus polymerse (HCVpol), the central catalytic channel is enclosed by additional loops ('fingertips') that connect the thumb and fingers, limiting the possibility of large-scale opening and closing motions as in DNA polymerases (13). Thus, in the absence of domain motion, the narrow template channel (Supplementary Figure S1b) is capable of accommodating ssRNA but not RNA duplexes. However, these motions, though not large in amplitude, likely exist, since both enzymes are capable of processing circular templates (14). Reorientation of the fingers and thumb would then be necessary in order to accommodate the wider template. Indeed structures of HCVpol have been solved in both the 'open' and 'closed' forms (15).

On the other hand, evidence of motion on a more local scale has also been found in RdRPs. Studies on the poliovirus polymerase (3Dpol) and also on other classes of nucleic-acid polymerases (HIV-1 reverse transcriptase, RB69 DNA-dependent DNA polymerase and T7 DNA-dependent RNA polymerase) have suggested that a step that leads to significant rate enhancement

*To whom correspondence should be addressed. Tel: +1 212 650 6049; Fax: +1 212 650 6107; Email: rghose@sci.ccny.cuny.edu

during the nucleotide addition cycle involves protonation of the pyrophosphate product facilitated by conformational changes in motif D (16). Other studies have hinted towards the influence of motions involving motif A on catalysis (17). An allosteric surface site that binds NTPs has also been located in HCVpol (18). This site, that is a target for a host of nucleotide-mimetic antivirals, is dynamically coupled to the catalytic site that is more than 30-Å away (19). Thus, dynamics both local and long-range, seem to be 'the missing link between structure and function' (12) in these ubiquitous enzymes.

Measurement, quantitative analyses and interpretation of nuclear spin relaxation data in solution provides the most promising route towards characterization of dynamics on multiple timescales (20) to complement the large amount of structural and biochemical data available on RdRPs. These studies have proven to be quite successful in revealing functional dynamics in other proteins. For example, in the case of adenylate kinase, the lid opening motions were noted to be rate limiting in the catalytic cycle of the enzyme (21). Similar conclusions were drawn for cyclophilin A where the measured exchange rate (k_{ex}) obtained from relaxation dispersion experiments, was found to be close to the sum of the forward and reverse rates of substrate *cis–trans* isomerization (22).

While the RdRPs are large (>55 kDa) and generally difficult to solubilize in high enough quantities under conditions suitable for NMR studies, recent advances in experimental methodology for both the backbone (23) and sidechains (24) coupled with the availability of cryogenic probe technology (25), provide great promise for the accurate measurement and interpretation of spin-relaxation data for these enzymes in solution. In our attempts to elucidate the role of dynamics along the catalytic cycle of RdRPs, in atomic detail, we have commenced NMR studies of ϕ6 P2. While an analysis of the dynamics of all backbone and sidechain nuclei remains our goal, as a first step, we present here an analysis of the spin-relaxation of multiple quantum (MQ) coherences involving ^{13}C and ^{1}H nuclei at the δ1 position of the Ile residues in P2 (26–28). We find that the enzyme is dynamic on multiple timescales, a behavior not immediately obvious from crystallographic analyses alone (9). These various motional modes that are active in apo P2, are perturbed by the presence of Mg^{2+} ions, substrate NTPs and short ssRNA, and provide insight into the dynamic nature of the initiation complex. The timescale of the lower frequency motional modes that involve several conserved functional motifs coincides with that relevant for catalysis as determined from kinetic analyses of representative RdRPs (29).

MATERIALS AND METHODS

Overexpression and Purification of ϕ6 P2

The ϕ6 P2 expression plasmid was constructed by PCR amplification of the pLM687 (30) plasmid that encodes of the cystoviral L segment with recombinant Pfu DNA polymerase (Stratagene) by using the following oligonucleotides—5′-GGTAAGCGCCATATGCCGAG GAGA-3′ and 5′-TACGAATTCCGGCATGATTACCT AGGCATTACA-3′ as upstream and downstream primers, respectively. The P2 gene fragment was digested with NdeI and EcoRI, and ligated to a digested pET28a(+) vector (Stratagene). N-terminal His_6-tagged full-length P2 was transformed into *Escherichia coli* BL21-DE3 (Stratagene) and grown overnight in 20 ml of unlabeled M9 medium prepared in 100% H_2O and supplemented with kanamycin (50 mg/l). Following overnight growth, the bacteria were adapted for growth in media containing progressively higher concentrations of D_2O from 10 to 100% at 37°C. The final overnight culture (20 ml grown in M9 medium prepared in 100% D_2O) was used to inoculate 1 l of M9 medium in 100% D_2O containing 3 g/l of U-[^{12}C,^{2}H]-glucose (CIL) and 1 g/l of $^{15}NH_4Cl$ (CIL) as the principal sources of carbon and nitrogen respectively. When the optical density at 600 nm reached ~0.6, 50 mg of 2-keto-3-d2-4-^{13}C-butyrate (CIL) was added into the growth medium. After 1 h of growth, the culture was placed on ice for 30 min and induced with 1 mM IPTG. The growth was continued for 20 h at 16°C. The cells were harvested by centrifugation at 5000 rpm and resuspended in lysis buffer containing 20 mM Tris–HCl (pH 7.2), 300 mM NaCl, 5 mM Imidazole and two tablets of Complete Mini EDTA-free protease inhibitor (Roche). The suspension was lysed by sonication and the lysate was centrifuged at 16 000 rpm for 30 min at 4°C. The soluble lysate was then loaded onto a nickel affinity column (Ni–NTA agarose, Qiagen), and washed extensively with buffer containing 20 mM Tris–HCl (pH 7.2), 300 mM NaCl, and 20 mM imidazole. The bound recombinant P2 was eluted with buffer containing 20 mM Tris–HCl (pH 7.2), 300 mM NaCl, 500 mM imidazole and then dialyzed against the NMR buffer that contained 20 mM bis-tris, 400 mM NaCl and 4 mM DTT at pH 6.5. The uniformly-^{15}N,^{2}H-Ile-δ1-^{13}C,^{1}H-labeled protein was concentrated by using Amicon Ultra-4 or Amicon Ultra-15 centrifugal concentrators (Millipore) for NMR analyses.

Assignment of Ile δ1 resonances

All NMR experiments were performed using a Varian Inova 600 MHz spectrometer equipped with a triple-resonance {^{1}H,^{13}C}-cryogenic probe capable of applying pulsed field gradients along the *z*-axis. Resonance assignment of the 25 Ile δ1 resonances was achieved using an Ile-to-Leu mutation strategy described below (Supplementary Figure S2). Twelve Ile-to-Leu triple mutants were designed specifically avoiding simultaneous mutation of Ile residues that were sequentially or spatially proximal in the same set. In addition 13 single Ile-to-Leu mutants were also created. Mutations were introduced into the cDNA corresponding to wild-type ϕ6 P2 using the QuikChange Site-directed Mutagenesis and QuikChange Multisite-directed Mutagenesis kits (Stratagene) using primers designed utilizing the QuikChange Primer Design Program (Stratagene). The mutations were confirmed by sequencing. The mutated plasmids were transformed

into *E. coli* BL21-(DE3)-RIPL competent cells (Stratagene) and each uniformly-^{15}N,^{2}H-Ile-δ1-^{13}C,^{1}H-labeled mutant P2 was overexpressed and purified as described previously. The resonances corresponding to mutated Ile δ1 positions vanished in an ^{13}C,^{1}H HMQC spectrum. Of 25 Ile-δ1 resonances, 15 were assigned using the strategy employing triple-mutants (see the legend to Supplementary Figure S2 for more details). However, some of these mutations resulted in protein misfolding and could not be used for assignments. Consequently, assignments for 8 of the remaining 10 Ile δ1 resonances were obtained using Ile-to-Leu point mutants. Resonances corresponding to Ile211 and Ile283 could not be unambiguously identified.

Chemical shift changes

The concentrations of Mg^{2+} (states **2–6**, Table 1), of GMPPNP (Sigma-Aldrich) (states **3**, **4** and **5**) and of GMPCPP (Jena Biosciences) (states **3A** and **6**), were held constant at 5, 4 and 4 mM, respectively. The concentrations of the ssRNA were maintained in 3.5–5-fold excess of the concentration of P2 (250–350 μM).

Scaled chemical shift changes ($\Delta\delta_{ij}$ in Hz) between states i and j (i, j = **1**, **2**, **3**, **3A**, **4**, **5**, **6**; Table 1) were calculated using the following equation

$$\Delta\delta_{ij} = \nu_0\sqrt{\left(\delta_{i,\,\mathrm{H}} - \delta_{j,\,\mathrm{H}}\right)^2 + \left(\frac{\gamma_{\mathrm{C}}}{\gamma_{\mathrm{H}}}\left(\delta_{i,\,\mathrm{C}} - \delta_{j,\,\mathrm{C}}\right)\right)^2} \quad i \neq j \qquad (1)$$

where $\delta_{i/j,\mathrm{C/H}}$ are the ^{13}C/^{1}H chemical shifts in states i/j in ^{13}C,^{1}H HMQC spectra and ν_0 is the spectrometer ^{1}H frequency in MHz (600 MHz in the present case).

NMR relaxation measurements

All relaxation experiments were performed at 25°C and 600 MHz using sweep-widths of 9000 and 1600 Hz in the direct (^{1}H, 512 complex points) and indirect (^{13}C, 32 complex points) dimensions respectively. The ^{13}C carrier was positioned at 13.15 ppm at the center of the Ile ^{13}Cδ1 resonances. P2 concentration varied from 250 to 350 μM for the cross-correlated relaxation measurements and was around 250 μM for the relaxation dispersion measurements. All fits to theoretical curves both for the relaxation analyses [Equations (2) and (4)] and for the fluorescence measurements [Equation (6)] were performed using in-house programs that utilize the ODRPACK subroutines (31). Errors in the fitted parameters were obtained from the inverse covariance matrices of the fits and included both the random as well as the model selection errors.

Table 1. Complexes of ϕ6 P2 utilized in this study

State	Complex
State **1**	P2
State **2**	P2, Mg^{2+}
State **3**	P2, Mg^{2+}, GMPPNP
State **4**	P2, Mg^{2+}, GMPPNP, 5′-UUUCC-3′
State **5**	P2, Mg^{2+}, GMPPNP, 5′-UUUUC-3′
State **3A**	P2, Mg^{2+}, GMPCPP
State **6**	P2, Mg^{2+}, GMPCPP, 5′-UUUCC-3′

Measurement of intra-methyl ^{1}H–^{1}H cross-correlation rates. In order to measure the intra-methyl ^{1}H–^{1}H dipole-dipole cross-correlated relaxation rate (η)(32), a set of two experiments were recorded. The signal intensity (I_A) in the first experiment (A) during a variable relaxation delay (T) depends only on spin-dynamics in the $I = 3/2$ manifold of the Ile δ1 methyl H_3 spin-system. In the second experiment (B), the signal intensity (I_B) is affected by spin-dynamics in the $I = 3/2$ and $I = 1/2$ manifolds. The cross-correlation rate (η) is related to the intensity ratio (I_A/I_B) in the following way (32):

$$\frac{I_{\mathrm{A}}}{I_{\mathrm{B}}} = \frac{-0.5\eta\tanh\left(\sqrt{\eta^2+\delta^2}\,T\right)}{\sqrt{\eta^2+\delta^2}\,T - \delta\tanh\left(\sqrt{\eta^2+\delta^2}\,T\right)} \qquad (2)$$

where δ depends on the ^{1}H–^{1}H cross-relaxation with external protons. Seven values of T = 1, 2, 4, 6, 8, 10 and 14 ms were used with 256 and 64 transients per t_1 point for experiments A and B, respectively. η and δ values were obtained by fitting the experimentally determined I_A/I_B ratio as a function of T to Equation (2). The order-parameters (S^2_{axis}) were calculated from the following equation (32) using the rotational correlation time (τ_C) (assuming that the rotational diffusion was isotropic) estimated from hydrodynamic modeling:

$$S^2_{\mathrm{axis}} = \frac{10}{9}\frac{r^6_{\mathrm{HH}}\eta}{\gamma^4_{\mathrm{H}}\hbar^2\tau_{\mathrm{C}}P_2(\cos(\theta_{\mathrm{HH}}))^2}$$
$$P_2(\cos(\theta_{\mathrm{HH}})) = \frac{3\cos\theta^2_{\mathrm{HH}} - 1}{2} \qquad (3)$$

where r_{HH} = 1.813 Å, θ_{HH} = 90° and all other symbols have their usual meaning.

Multiple–quantum relaxation dispersion. ^{13}C,^{1}H multiple quantum relaxation dispersion curves were obtained for states **1–6** (Table 1) at 600 MHz using the pulse sequences developed by Korzhnev *et al*. (33). Fifteen values of the RF–field strength ($\nu_1 = 1/2\tau_{\mathrm{CPMG}}$, where τ_{CPMG} is the spacing between successive π pulses) = 31.25, 62.5, 93.75, 125.0, 156.25, 187.5, 250.0, 312.5, 375.0, 437.5, 500.0, 625.0, 750.0, 875.0 and 1000 Hz were used with a constant relaxation delay of 32 ms. 128 transients were collected per t_1 point. Data at each field were acquired in an interleaved fashion with all ν_1 values collected prior to t_1 incrementation in order to minimize possible errors resulting from sample heating and/or precipitation and to increase the accuracy of the fitted exchange parameters. All relaxation dispersion data were analyzed assuming exchange between two chemically distinct sites A and B with an exchange rate $k_{ex} = k_{A\to B} + k_{B\to A}$, where $k_{A\to B}$ and $k_{B\to A}$ are the rates for the forward and reverse processes, respectively. In the limit of fast exchange, when $k_{ex} >> (\Delta\omega_{H\Delta}\omega_C)^{1/2}$ (where $\Delta\omega_H = |\omega_H(A) - \omega_H(B)|$ and $\Delta\omega_C = |\omega_C(A) - \omega_C(B)|$ are the differences between the chemical shifts of the two states for the ^{1}H and ^{13}C nuclei, respectively) and when $\Delta\omega_H \to 0$, the effective

multiple–quantum relaxation rate ($\Gamma_{MQ,eff}$) for a given RF–field, ν_1 is given by (33,34)

$$\Gamma_{MQ,eff}(\nu_1) = \Gamma_{MQ}(\infty) + \frac{\xi}{k_{ex}}\left(1 - \frac{4\nu_1}{k_{ex}}\tanh\left(\frac{k_{ex}}{4\nu_1}\right)\right) \quad (4)$$

$\xi = 2p_A(1-p_A)\Delta\omega_H\Delta\omega_C$, p_A is the fractional occupancy of state A (the fractional occupancy of state B, $p_B = 1-p_A$) and $\Gamma_{MQ}(\infty)$ is the multiple–quantum relaxation rate at infinite field strength i.e. the value of $\Gamma_{MQ,eff}$ in the absence of chemical exchange. The k_{ex} values were obtained as one of the parameters in a three–parameter [k_{ex}, $\Gamma_{MQ}(\infty)$ and ξ] fit of the experimental dispersion curves to Equation (4).

A point to be made here is that for practical considerations, using Equation (4) should not result in substantial errors in k_{ex} values provided that the product, $\Delta\omega_{H\Delta}\omega_C$, is small and the dynamic timescale lies in the fast exchange limit. However, errors in $\Gamma_{MQ}(\infty)$ and ξ, using this simplified approach, are larger and correlated with each other. Therefore we do not attempt to interpret $\Gamma_{MQ}(\infty)$ and ξ values obtained in the present study.

Fluorescence measurements

All fluorescence anisotropy experiments were performed using single-stranded RNA oligos (5′-UUUCC-3′ and 5′-UUUUC-3′) labeled at the 5′-end with 6-carboxyfluorescein. Oligos were purchased PAGE purified from Dharmacon RNAi Technologies. Experiments were performed using a Panvera Beacon 2000 fluorescence anisotropy system. Fluorescence intensity data were acquired by passing the emission following an excitation at 490 nm through a 520 nm cutoff filter. A 10 s integration time was used for four combinations of the horizontal (H) and vertical (V) polarization filters. The measured intensities using parallel (I_{VV}) and perpendicular (I_{VH}) polarizer settings were converted into fluorescence anisotropy using the following equation:

$$A = \frac{I_{VV} - I_{VH}}{I_{VV} + 2I_{VH}} \quad (5)$$

Anisotropy values (A) were measured in the presence of increasing amounts of P2. Values of the dissociation constant (K_d) were obtained by fitting the dependence of A on P2 concentration using the following equation:

$$A(C) - A(0) = (A_\infty - A(0)) \times \frac{K_d + C_{RNA} + C - \sqrt{(K_d + C_{RNA} + C)^2 - 4C_{RNA}C}}{2C_{RNA}} \quad (6)$$

where $A(C)$ is the anisotropy when the concentration of P2 is C and A_∞ is the limiting anisotropy value. The concentration of RNA (C_{RNA}) was kept constant at 5 nM. All experiments were performed at pH 6.5 in the NMR buffer. Absence of non-specific binding to the fluorescein moiety was confirmed by measuring A values of fluorescein alone (300 nM) and in the presence 40 and 400 μM P2.

In order to measure the affinity of the GTP-analogs GMPPNP and GMPCPP towards P2, tryptophan (ϕ6 P2 contains 12 Trp residues) fluorescence spectra were obtained using a Spex Fluorolog-3 (Horiba Jobin Yvon) spectrometer with excitation and emission slits set to 1.6 nm. Fluorescence emission spectra (300–450 nm) were acquired in 0.5-nm steps and signal-averaged over three scans. Emission intensities were obtained by averaging the values at the maximum ± 4 nm. The excitation wavelength was set to 282 nm for each addition of either GMPCPP or GMPPNP to the protein sample in NMR buffer. Apparent K_d values were obtained by using fits to an analog of Equation (6) with the anisotropy values replaced by the corresponding emission intensities, the C_{RNA} by the concentration of P2 (held constant at 10 μM) and C by $C_{GMPNP/GMPCPP}$ representing the variable concentration (0–2.5 mM) of the GTP analogs.

Hydrodynamic modeling

The diffusion tensor for full-length P2 was estimated by utilizing the bead model as implemented in the HYDRONMR program (35). The effective radius of the atomic elements was set to 3.2 Å, the temperature to 298.15 K and the viscosity to 9.11 cP. The minibead solvent shell radius was calculated automatically. The atomic coordinates of P2 were obtained from structures with the following PDB IDs: 1HHS, 1HHT, 1HI0, 1HI8, 1UVI, 1UVJ, 1UVL, 1UVM and 1UVN.

RESULTS AND DISCUSSION

The principal focus of this work is to ascertain the functionally relevant motions in P2 for multiple states along its enzymatic pathway. The motions that are capable of influencing catalysis in RdRPs are typically slow, occurring on a millisecond-to–microsecond (μs–ms) timescale (29). Given this timescale, these motions are likely to involve relatively large structural segments and are thus expected to be non–local. This is in contrast to more local, fast dynamics on a picosecond–to–nanosecond (ps–ns) timescale involving only a small group of atoms. While characterizing dynamics in atomic detail, on both the ps–ns and μs–ms timescale, remains our goal, in the present work we use the δ1 position of the 25 Ile residues in P2 as probes of motional changes along its catalytic cycle. Given the near uniform distribution of the Ile residues over the structural domains (Figure 1a) and the key functional motifs (Figure 1b) of P2, this approach should provide valuable insight not only into the large amplitude μs-ms timescale motions in P2 that likely affect catalysis, but also into the local (ps–ns) flexibility of the catalytic motifs.

Chemical shift assignment

$^{13}C,^{1}H$ HMQC spectra of uniformly-deuterated,Ile-δ1-[$^{13}C,^{1}H$]-labeled P2 showed excellent dispersion and all 25 expected Ile δ1 ^{13}C, ^{1}H resonances were seen/resolved (Figure 1c). Resonance assignments were carried out using a set of Ile-to-Leu single and triple mutants as described in the 'Materials and Methods' section. The methodology employing triple-mutants has been described in detail in the Supplementary Data (see the legend to Supplementary Figure S2). In all, 23 of 25 Ile resonances could be

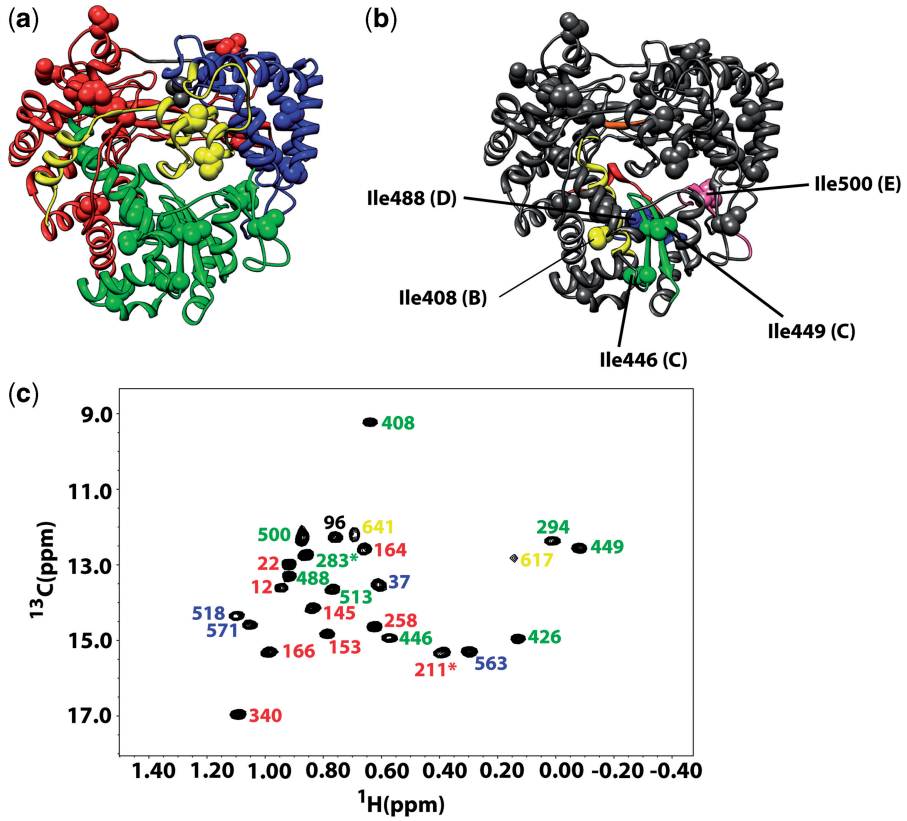

Figure 1. (**a**) Distribution of Ile residues over the P2 tertiary structure. The fingers (1–30, 104–276, 333–397), thumb (37–91, 518–600), palm (277–332, 398–517) and C-terminal domains (601–664) are colored red, blue, green and yellow respectively. The Ile residues are shown as spheres and colored according to the domains they belong to: fingers (12, 22, 145, 153,164, 166, 211, 258 and 340); thumb (37, 518, 563 and 571); palm (283, 294, 408, 426, 446, 449, 488, 500 and 513) and C-terminal (617 and 641) domains. Ile96 that lies on the fingertips is colored dark gray. (**b**) Conserved RdRP sequence motifs in P2. Motif A (324–334, red), motif B (394–413, yellow), motif C (445–461, green), motif D (475–488, blue), motif E (493–505, pink) and motif F (268–272, orange) are shown. The Ile residues that lie on motifs A–F are colored accordingly and labeled. Motif C contains the ^{452}G/SDD^{454} sequence motif characteristic of RNA and DNA polymerases. (**c**) Assigned ^{1}H,^{13}C HMQC spectrum of uniformly deuterated Ile-Cδ1-^{13}C,^{1}H-labeled P2. The spectrum was acquired at a ^{1}H field strength of 600 MHz at 25°C in a buffer containing 20 mM bis–tris, 400 mM NaCl, 4 mM DTT at pH = 6.5. The resonances have been labeled according to the color scheme described in the (a). Resonances corresponding to Ile211 and Ile283 could not be unambiguously assigned using the Ile-to-Leu mutation strategy and these assignments indicated by asterisk should be considered tentative.

unambiguously assigned using this strategy. Resonances corresponding to Ile211 and Ile283 (indicated by asterisk in Figure 1c) could only be tentatively assigned and relaxation data for these residues were not interpreted further.

Choice of binary and ternary complexes of P2

We analyzed the spin relaxation rates of the Ile δ1 positions for P2 in the apo state, in complex with Mg^{2+}, with GTP analogs—GMPPNP and GMPCPP, and two different 5-nt ssRNA constructs. A total of seven distinct states (states **1**, **2**, **3**, **3A**, **4**, **5** and **6**, Table 1) including binary and ternary complexes, were studied. The RNA construct, 5′-UUUCC-3′, chosen for states **4** and **6**, corresponds to the final 5 nt from the 3′-end of the minus-strands (called s^- and m^-) of the small and medium segments of the three-segmented (S, M and L for small, medium and large) double-stranded RNA (dsRNA) genome of cystoviruses. Biochemical data for P2 reveals that transcription is far more efficient for the s^- and m^- strands compared with that of l^- (that contains a 5′-UUUAC-3′ sequence at the 3′-end) suggesting a role for the 3′-end sequence (more specifically of the penultimate nucleotide from the 3′-end) on the ability of ssRNA to be processed by P2 (6). The second 5-nt ssRNA construct chosen for the present study, differed in sequence from the first, only at the penultimate position from the 3′-end (U instead C–5′-UUUUC-3′), while introducing a minimal size differential. Choice of this construct provides an additional advantage that is described at length in the following paragraph.

The choice of the ternary complexes of P2 with substrate (Mg^{2+}/GTP analogs) and ssRNA warrants some discussion (Figure 2). For RdRPs that initiate RNA synthesis *de novo* i.e. without the use of a primer, the initiation NTP acts as a 1-nt primer and base-pairs with the extreme 3′-nt (T1) of the template forming the first nucleobase (D1) from the 5′-end of the daughter strand. The second substrate NTP (D2) base pairs with the penultimate template nucleotide from the 3′-end (T2). Formation of a stable initiation complex requires both T1–D1 and T2–D2 base-pairing to occur. The first phosphodiester bond is thus formed between D1 and

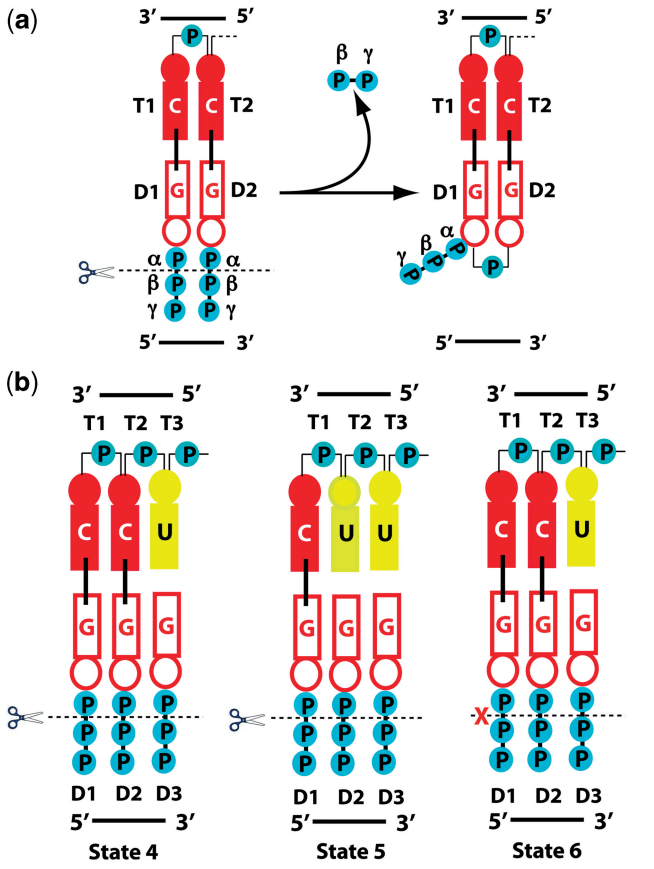

Figure 2. (**a**) Formation of a stable initiation complex results from the proper base pairing of the template bases T1 (C) and T2 (C) (numbered 3′→5′) with the substrate (GTP analog) bases D1 (G) and D2 (G). Nucleophilic attack by the 3′-OH of D1 and cleavage between the α and β−phosphate groups of D2 (represented by the dotted line), results in the formation of the first 3′–5′ phosphodiester bond of the daughter chain between D1 and D2 (numbered 5′→3′), releasing pyrophosphate. The requirements for the reaction to proceed are thus, (1) proper T1–D1 and T2–D2 base pairing (indicated by solid lines) and (2) cleavability of the substrate (indicated by dashed lines) between the α,β−phosphates. (**b**) Schematic representation of the three ternary complexes (states **4**, **5** and **6**) between P2, substrate GTP analogs and 5-nt ssRNA templates. State 4: T1 (C)-D1 (G) and T2 (C)-D2 (G) are correctly base-paired, the substrate GMPPNP is α−β cleavable and the reaction proceeds for one cycle generating 5′-PPP-G-P-3′. The reaction subsequently stalls since the base (D3, A) complementary to T3 (U) from ATP (or an analog) is not available. State 5: The substrate GMPPNP is α−β cleavable but proper base paring between T2 (U) and D2 (G) cannot occur. State 6: T1–D1 and T2–D2 properly base pair, however the substrate, GMPCPP, is not is α−β cleavable and the reaction cannot proceed.

D2 with the cleavage of the latter between the α and β−phosphates releasing pyrophosphate (shown schematically in Figure 2a, also see Supplementary Figure S3). The process continues with each incoming substrate nucleotide (CTP, UTP, ATP or GTP) complementary to the corresponding template nucleobase (36). Thus, among the ternary complexes studied here, state **4** (Table 1, Figure 2b) represents a dead-end or stalled complex where the first phosphodiester bond between D1 and D2 can form since GMPPNP is a viable substrate for P2 (Supplementary Figure S3) given the fact that it can be cleaved between the α and β phosphates (37). However, additional polymerization beyond the one-nucleotide addition cycle and formation of a 2-nt daughter chain (5′-PPP-G-P-G-3′) becomes extremely inefficient, as the substrate nucleotide (A from ATP or an ATP-analog) complementary to T3 (U) is unavailable. Examples of stalling through nucleotide deprivation in ϕ6 P2 has been described in the literature (38) and characterized structurally (10). In state **5** (Table 1) a complex capable of forming a stable initiation platform cannot form since the complementary nucleotide D2 (A from ATP or analog) for T2 (U) is unavailable (Figure 2b). State **6** (Table 1), on the other hand, represents a stable initiation complex, stabilized by proper base-pairing of D1 with T1 and D2 with T2 (D1,2 = GMPCPP and T1,2 = C). However the phosphodiester linkage between D1 and D2 cannot form since in GMPCPP the bond between the α and β phosphates cannot be cleaved (Figure 2b and Supplementary Figure S3).

Fast dynamics

Prior to probing the catalytically relevant μs-ms timescale, we investigated the local rigidity of the Ile δ1 positions on the fast ps–ns timescale. Thus, beginning with the apo enzyme (state **1**), the difference between the relaxation rates of the fast and slow relaxing coherences corresponding to the $I = 3/2$ manifold of the methyl H_3 spin-system at each Ile δ1 positions, was measured. The extracted difference relates to the intra-methyl ^1H–^1H dipole–dipole cross-correlation rate (η). This rate being independent of chemical exchange to first-order (27,28) is therefore uncontaminated by the effects of slow conformational dynamics and represents an accurate measure of local dynamics on the fast, ps–ns timescale through its relationship with the order parameter, S^2_{axis} [Equation (3)]. For residues that are highly disordered on the ps–ns timescale, S^2_{axis} values are close to 0, and residues that are ordered on this timescale display S^2_{axis} values that are close to 1.

η values for 21 of 25 Ile [^1H,^{13}C]-δ1 resonances were analyzed in detail for states **1** through **4**. Signals corresponding to Ile617 and Ile641 from the C-terminal domain were weak and excluded from the analysis as were those belonging to Ile211 and Ile283. Representative fits to Equation (2) (see 'Materials and Methods' section) and the η values for the 21 Ile resonances for the four states analyzed are shown in Figure 3.

Prior to the availability of backbone ^{15}N, ^1H assignments and the analysis of backbone ^{15}N relaxation rates, we relied on hydrodynamic calculations (35) to estimate the nature of the rotational diffusion tensor (see 'Materials and Methods' section) of P2. This was required to justify the use of Equation (3) that assumes isotropic rotational diffusion with a single correlation time (τ_C) and also to utilize the τ_C value to convert the experimental η to the more readily interpretable S^2_{axis} using Equation (3). These calculations predicted a nearly isotropic diffusion tensor [$2D_{zz}/(D_{xx}+D_{yy}) = 1.07 \pm 0.03$] with a corresponding τ_C of 40.15 ± 0.76 ns. Thus using a τ_C value of 40 ns we estimated S^2_{axis} values for states **1–4** using Equation (3).

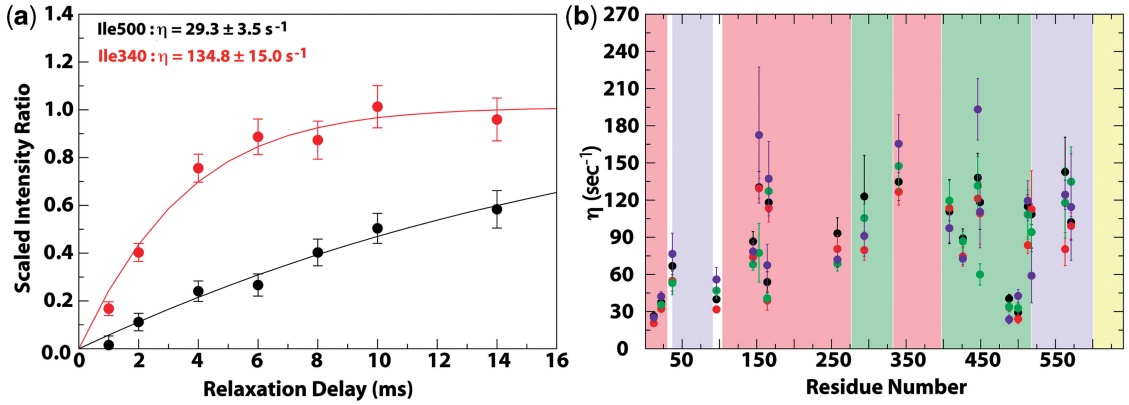

Figure 3. (**a**) Representative fits to Equation (2) for Ile340 and Ile500 are shown for P2 in the apo state (state **1**). The scaling factor used in the *y*-axis is the ratio (4) of the number of scans used in experiments A and B. (**b**) η values for the Ile residues in P2 are plotted against residue number. η values for states **1**, **2**, **3** and **4** are represented by black, red, green and purple circles respectively. The regions corresponding to the fingers, thumb, palm and C-terminal domains are shaded red, blue, green and yellow respectively. Data corresponding to Ile211, Ile283, Ile617 and Ile641 were not analyzed.

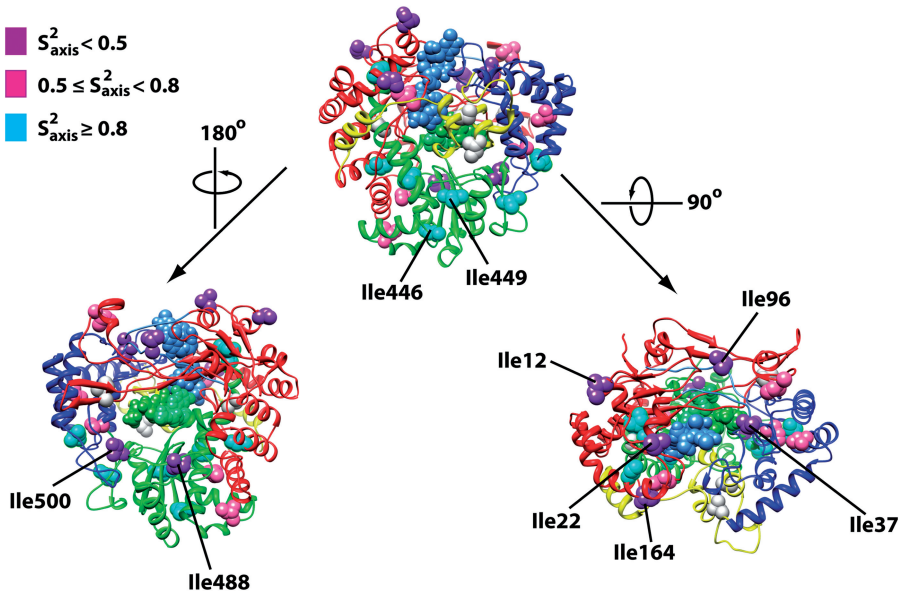

Figure 4. S^2_{axis} values for the Ile Cδ1 positions in apo-P2 (state **1**). The Ile residues are indicated by spheres colored according to their respective S^2_{axis} values. Three views of P2 are shown and key residues labeled. Residues for which data could not be analyzed (Ile211, Ile283, Ile617 and Ile641) are indicated by light grey spheres. The two substrate molecules are shown in green and the template in blue.

Apo P2 (Figure 4) displayed an average S^2_{axis} value of 0.63 ± 0.27 (10% trimmed — 0.60 ± 0.22) with the highest degree of order seen for the palm domain residues located in and around the catalytic site including those that form a part of motif C (445–461; Ile446, 0.96 ± 0.14 and Ile449, 0.82 ± 0.15) that bears the conserved catalytic DD motif (Asp453, Asp454). On the other hand, the most dynamic Ile residues were located on the edge of the template tunnel at the top the fingers domain—Ile12 (0.18 ± 0.01), Ile22 (0.26 ± 0.01), and Ile164 (0.37 ± 0.06); Ile37 (0.46 ± 0.07) on the thumb domain; and Ile96 (0.28 ± 0.02) located on the fingertips. This mobility at the entrance to the template pore could be the result of fast fluctuations at the top of the fingers and the thumb domains. The other parts of the fingers and thumb were relatively well ordered on the fast timescale. The other residues that were disordered on the fast timescale included Ile488 (0.28 ± 0.02, motif D) and Ile500 (0.20 ± 0.02, motif E) near the catalytic site at the entrance of the substrate channel.

An analysis of the S^2_{axis} values in states **2–4** revealed small but significant changes in the dynamic nature of several residues compared with the apo state. While the overall patterns of fast dynamics were generally similar, some very large variations were seen especially around the catalytic site for the motif C residues Ile446 and Ile449. Ile449, located near the top of the β-hairpin bearing the catalytic Asp residues displayed increased disorder in the complex with substrate GMPPNP/Mg^{2+} (state **3**, S^2_{axis} = 0.42 ± 0.06 compared with 0.82 ± 0.15 for

state **1**). This motion is indicative of local conformational diversity of the top of the hairpin and likely originates from the continuous remodeling of the catalytic cavity to facilitate stabilizing local interactions with a variety of templates and substrates. Ile446, located at the base of the hairpin became highly ordered in state **4** ($S^2_{axis} = 1.34 \pm 0.27$). This extreme rigidity near the catalytic site possibly reflects a distinct state for the stalled enzyme. Notably, Ile449 ($S^2_{axis} = 0.77 \pm 0.33$) is also ordered in state 4. As will be discussed at length below, both the analysis of chemical shift perturbations as well as the dynamic characteristics on the μs-ms timescale also seemed to indicate that state **4** was quite different from all other states considered.

While the errors in the experimental η values (and consequently the S^2_{axis} values) were relatively large, the overall rigidity of the stalled complex (state **4**, $S^2_{axis} = 0.64 \pm 0.20$, 10% trimmed—$0.57 \pm 0.18$) while comparable with that of the apo enzyme (state **1**) was higher than both state **2** (Mg^{2+}, $S^2_{axis} = 0.54 \pm 0.25$, 10% trimmed—$0.51 \pm 0.20$) and state **3** (GMPPNP/Mg^{2+}, $S^2_{axis} = 0.57 \pm 0.27$, 10% trimmed—$0.52 \pm 0.21$). The increased fluctuations on the fast timescale in the Mg^{2+}/GTP complexes could be an indication of conformational fine-tuning of the enzyme to facilitate the processing of a variety of ssRNA templates and substrate NTPs.

Thus, considering the S^2_{axis} values of all four states (states **1–4**) together, the highest degree of flexibility on the ps–ns timescale was seen for the Ile residues in close proximity to the entry portals for the substrate NTPs and the template ssRNA. This was in contrast to the high rigidity seen for the two Ile residues located on the catalytic motif C, except for the increased disorder at the top of this motif in the Mg^{2+}/GMPPNP-loaded state (state **3**). Altogether, the fast dynamics seems connected to loading of both substrates and templates. This increased dynamics likely helps modulate local interactions allowing a variety of substrates and templates (with differences in local structure, e.g. variation in possible hydrogen-bond donors or acceptors) to be processed efficiently.

Binding affinity towards ssRNA and GTP-analogs

The ternary complexes (P2/Mg^{2+}/GMPPNP/ssRNA) studied here involved two different ssRNA constructs. Prior to analyzing the dynamics on the μs–ms timescale it was necessary to confirm that perceived motional differences (as inferred from differences in k_{ex} values) between the complexes were not related to exchange between substrate/template-bound and free forms of P2 i.e. to simple on/off processes. To estimate the exchange contributions from these processes, knowledge of the affinities of the two GTP analogs (GMPPNP and GMPCPP) and the two different RNA constructs, used in this study, towards P2, was required.

In order to measure the binding affinity of the two 5-nt ssRNA constructs towards P2 we performed fluorescence anisotropy measurements using 5′-fluorescein tagged RNA. Fluorescein, in its singly protonated form ($pK_a = 6.4$) has a reduced molar absorptivity ($\varepsilon = 29000\,M^{-1}cm^{-1}$) compared with the corresponding dianionic form ($\varepsilon = 76900\,M^{-1}cm^{-1}$) (39) that is the dominant species above pH = 7. However, we chose to perform these experiments using the NMR buffer (pH = 6.5) for consistency with the relaxation studies for states **4, 5** and **6**. In spite of the reduced fluorescence, changes in fluorescence anisotropy could be monitored with a high degree of accuracy and the resultant binding isotherms could be fit to Equation (6) to obtain apparent K_d values (Figure 5). These studies revealed that P2 has a higher affinity for 5′-UUUUC-3′ ($K_d = 6.6 \pm 0.4$ μM) than for 5′-UUUCC-3′ ($K_d = 50.0 \pm 1.7$ μM). No significant changes in binding affinity were noted in the presence of GMPPNP. Based on the binding affinities of the ssRNA templates and their concentration (~mM) in the NMR experiments one can estimate a $k_{ex} = k_{on}(C_{RNA}+K_d) \sim 10^5\,s^{-1}$ for exchange between the RNA-bound and free states of P2 assuming a diffusion limited on-rate. This value is about two orders of magnitude higher than the largest k_{ex} values ($\sim 10^3\,s^{-1}$) described below. Thus these simple on/off processes are too fast to contribute to the k_{ex} values measured from the relaxation dispersion experiments.

The binding affinities of the two GTP analogs towards P2, as estimated from tryptophan fluorescence quenching (data not shown) were quite similar (GMPPNP, $K_d = 317 \pm 31$ μM, GMPCPP, $K_d = 271 \pm 31$ μM) and comparable to that seen in other RdRPs (40). Here again, the expected k_{ex} values for simple on-off processes were expected to be 50- to a 100-fold higher than the highest k_{ex} values obtained from the relaxation dispersion experiments.

Slow dynamics

In order to investigate dynamics on the μs-ms timescale in P2 we performed an analysis of the dependence of the Ile-Cδ1 ^{13}C,^{1}H multiple-quantum (MQ) relaxation rates ($\Gamma_{MQ,eff}$) on the strength (ν_1) of an applied radiofrequency (RF) field (MQ relaxation dispersion) (33). These rates can be measured with high sensitivity in large proteins where traditional single-quantum (SQ) relaxation dispersion experiments are likely to fail (33). When the exchange

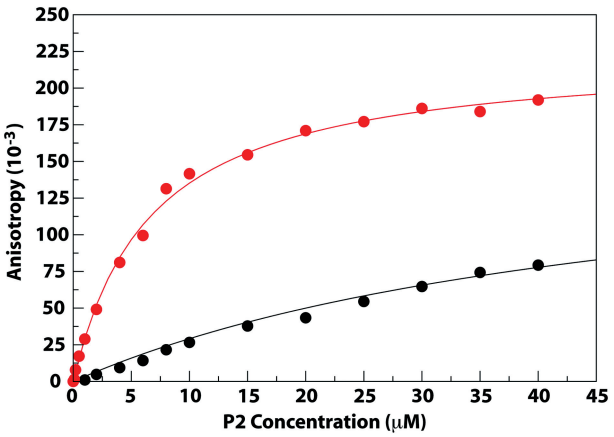

Figure 5. Binding affinity of the 5-nt ssRNA constructs towards P2. Data for 5′-UUUCC-3′ (black) and 5′-UUUUC-3′ (red) are shown. Solid lines represent theoretical curves obtained from fits to Equation (6) and circles represent the experimental data points.

rate (k_{ex}) is much greater than ν_1, the $\Gamma_{MQ,eff}$ values are essentially field-independent. However, when k_{ex} and ν_1 are of comparable magnitude, $\Gamma_{MQ,eff}$ becomes dependent on ν_1, reaching a field-independent limiting value [the inherent relaxation rate, $\Gamma_{MQ}(\infty)$] in the limit $\nu_1 >> k_{ex}$. The dependence of $\Gamma_{MQ,eff}$ on ν_1 is extremely complex and cannot, in general, be treated using the Carver-Richards formalism used for SQ relaxation (33). However, such an exact treatment requires high-quality data at multiple static magnetic fields. In the fast exchange regime, however, when the chemical shift differences between states A and B (see 'Materials and Methods' section) for the two nuclei participating in the MQ coherence, is small, a simple functional form may be used to extract k_{ex} values [Equation (4)] (34). We use this approach in the present case especially since the chemical shift changes seen (assuming that these changes are reflective of the difference between the two states) are sufficiently small so that the fast exchange condition $k_{ex} >> (\Delta\omega_H \Delta\omega_C)^{1/2}$ (where $\Delta\omega_H$ and $\Delta\omega_C$ are the chemical shift differences for ^{1}H and ^{13}C nuclei, respectively) was maintained in all of the cases analyzed below. Additionally, in this i.e. the fast exchange limit, MQ relaxation dispersion is uniquely sensitive to slow dynamics providing added incentive in choosing MQ relaxation over corresponding SQ relaxation measurements (41). Under the experimental conditions used here, k_{ex} values in the 100–2500 s^{-1} range can be determined with an acceptable degree of accuracy.

For apo-P2 (state **1**) statistically significant k_{ex} values could be obtained for eight Ile residues by fitting the MQ dispersion data to Equation (4). These values that varied from 449 to 1690 s^{-1} (Table 2), could be broadly classified into two distinct groups—group I that had higher exchange rates (k_{ex}) implying motion on a faster timescale (mean $k_{ex} = 1510 \pm 168\ s^{-1}$) and group II consisting of residues that were mobile on a slower timescale (mean $k_{ex} = 600 \pm 87\ s^{-1}$).

Group I consisted of two Ile residues that line one side of the entrance to the template tunnel (Ile37, Ile96) and one (Ile641) on the C-terminal domain (Figure 6a). k_{ex} values for the C-terminal Ile617 could not be extracted accurately due to extremely low S/N ratio for the corresponding resonance. However, visual inspection of the field-dependence of $\Gamma_{MQ,eff}$ suggested a k_{ex} value characteristic of a group I residue. In RdRPs, such as P2, that initiate RNA synthesis *de novo*, the absence of a primer requires additional interactions of the template ssRNA with the RdRP to stabilize the initiation complex. These interactions in P2 occur with a 'priming loop' located on the C-terminal domain and containing a conserved aromatic residue (Y630 in ϕ6 P2) (9). In addition, the accepted model for the exit of the newly synthesized daughter strands from the catalytic cavity involves motion of the C-terminal domain (9). It thus stands to reason that the conformational dynamics involving the C-terminal domain would be synchronized with those that allow the entry of ssRNA into the template tunnel. We therefore hypothesize that these faster motions are designed to facilitate entry of template and exit of the daughter chains in a coordinated fashion in line with the currently accepted model for RNA entry and egress (9). Extensive studies of the effects of mutations of key residues at the rim of the template tunnel and the C-terminal domain are available (42,43). However interpreting the effects of these mutations in terms of functional motions in a simple way is difficult. For example, the rim mutant K30A has reduced transcriptional activity but this may partially be explained by its reduced affinity for RNA. Replacing the priming loop ^{630}YSW^{632} (on the C-terminal domain) by a smaller and more dynamic GSG sequence leads to enhanced transcription, though this increase may also be attributed to back-priming as opposed to *de novo* RNA synthesis (42,43). A similar effect is obtained using the mutant E634Q which is expected to lead to a more dynamic C-terminal domain due to disruption in a salt-bridge with K144. Since this mutant has smaller (~20%) back-priming activity compared to the GSG mutant, enhanced mobility of the C-terminal domain does seem to play a role in transcriptional efficiency (43).

Group II consisted of Ile164, Ile258, Ile488, Ile500 and Ile563. Of these residues, Ile488 (motif D), Ile500 (motif E) were located in and around the catalytic motifs on the palm and Ile563 on the base of the thumb (Figure 6a). Ile164 is located in the so-called plough region (Figure 6a). It has been shown that plough mutants enhance transcriptional activity though they do not have any significant effect on template binding (43). This is consistent with the nature of motions displayed by Ile164 with the k_{ex} being smaller than those of the group I residues.

Table 2. Exchange rates (k_{ex} in s^{-1}) determined from Ile [^{13}Cδ1, ^{1}Hδ1] multiple quantum relaxation dispersion

State	Ile37	Ile96	Ile164	Ile258	Ile449	Ile488	Ile500	Ile563	Ile641
1	1481 ± 118	1358 ± 109	600 ± 142	550 ± 104	ND	562 ± 179	690 ± 40	449 ± 123	1690 ± 301
2	1292 ± 86	1537 ± 142	210 ± 109	311 ± 74	[a]	577 ± 61	1719 ± 368	418 ± 241	[a]
3	1112 ± 88	1315 ± 92	855 ± 136	450 ± 54	414 ± 179	425 ± 51	1042 ± 139	417 ± 79	1344 ± 110
4	[b]	ND	ND	ND	ND	853 ± 118	1811 ± 185	ND	[a]
5	1253 ± 104	1549 ± 148	522 ± 226	336 ± 116	[a]	528 ± 49	1431 ± 96	424 ± 101	[a]
3A	1214 ± 207	2105 ± 430	ND	ND	[a]	679 ± 93	767 ± 35	ND	[a]
6	1811 ± 522	ND	ND	ND	451 ± 181	671 ± 145	972 ± 186	ND	[a]

Residues for which dispersion profiles were flat i.e. those which had $\Gamma_{MQ,eff}$ values independent of the RF-field strength (ν_1) are indicated by 'ND'.
[a]Analysis of these resonances was not performed due to poor signal-to-noise.
[b]Quantitative fits to obtain k_{ex} values could not be performed for Ile37 in state **4** due to extensive line broadening indicative of a departure from the fast exchange regime. $\Delta\Gamma_{MQ,eff} = \Gamma_{MQ,eff}$ (31.25 Hz) − $\Gamma_{MQ,eff}$ (1000 Hz) ~15 s^{-1}.

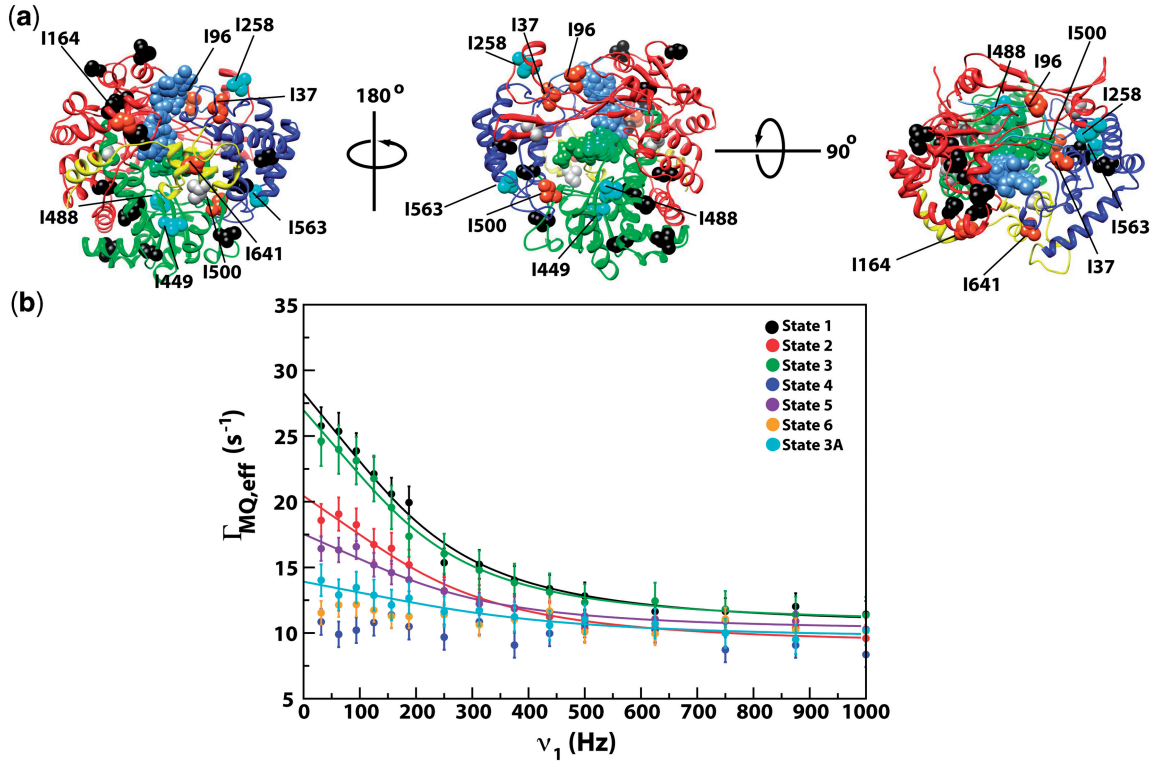

Figure 6. (**a**) Results of ^{13}C, ^{1}H multiple-quantum relaxation dispersion experiments. Ile δ1 positions that have detectable k_{ex} values are displayed on the tertiary structure of P2. Data for state **3** is shown as a representative example. Group I residues are shown in orange and group II residues are shown in cyan. Ile164 that has a k_{ex} value that is intermediate between group I and II for this state, is also shown in orange. Ile residues which had $\Gamma_{MQ,eff}$ values independent of the ν_1 field are depicted as black spheres. Data for Ile211, Ile283 and Ile617 were not analyzed in detail in any of the 7 states. These residues are indicated by light grey spheres. The two substrate molecules are shown in green and the template in blue. (**b**) Multiple-quantum dispersion data for Ile96 for all seven states are shown. Experimental data are represented by the circles and theoretical curves resulting from fits to Equation (4) are shown by solid lines. Theoretical curves are not shown for states **4** and **6**, where $\Gamma_{MQ,eff}$ is independent of the applied RF-field strength (ν_1).

Additionally, given that the motion of Ile164 occurs on a similar timescale as the catalytic site residues suggests some degree of coupling of the plough region to the active site and therefore to the transcriptional activity. Ile258 is located on the diametrically opposite end of the fingers (Figure 6a) suggesting that the group II motions represent dynamic coupling of the outer edges of the fingers to the active site. Given that this motional timescale was slower than that seen for group I residues (putatively involved in RNA entry and egress), they could be expected to be rate limiting, if indeed they are catalytically relevant. A recent kinetic study on the poliovirus RdRP 3Dpol (29), suggested several steps involving conformational changes that are likely to play a role in catalysis. These included: (i) a conformational transition in the RdRP/NTP/RNA ternary complex to an activated state primed for catalysis (expected k_{ex} ~800 s^{-1}), (ii) a transition from the activated complex to an activated product complex with pyrophosphate, the central reaction in the nucleotide addition cycle (expected k_{ex} ~895 s^{-1}), and (iii) a deactivation of the product complex (k_{ex} ~500 s^{-1}). The timescales associated with these three steps are consistent with the second, slower timescale seen in the present study (group II). The small differences in the predicted k_{ex} values between these three steps would make it difficult to pinpoint the exact conformational transition/s corresponding to the slower timescale. It is most likely that all of these transitions contribute to the distribution in k_{ex} values for the group II residues. However, the conjecture that these motions could be rate limiting in catalysis is reinforced by the detection of k_{ex} values in the 500–800 s^{-1} i. e. group II range for residues on several catalytic motifs, most notably in the Motif C residue Ile449 in the P2/Mg^{2+}/GMPPNP complex (state **3**) and in the stable initiation complex (state **6**) discussed below.

For state **2** (P2 + Mg^{2+}), as expected, no major changes in dynamic timescales are seen within group I (1516 ± 168 s^{-1}) or group 2 (379 ± 157 s^{-1}) residues. However, Ile500 that was a group II residue for state **1** now showed dynamics characteristic of group I (Table 2), accompanied by the largest $\Delta\delta_{1,2}$ [Equation (1)] between states **1** and **2** (19 Hz). This is not unexpected since Ile500 is within 4 Å of the divalent metal-binding sites. Comparatively large $\Delta\delta_{1,2}$ values were also seen for Ile164 (13 Hz), Ile449 (11 Hz) and Ile488 (14 Hz). All of these residues, with the exception of Ile164, were located at the catalytic center reinforcing the notion of long-range coupling of the plough region (where Ile164 is located) with the catalytic site.

For state **3**, a similar timescale separation was seen for group I (1134 ± 203 s^{-1}) and group II (427 ± 164 s^{-1}) residues. However, Ile164 now displayed a higher k_{ex}

value that was closer in magnitude to that for Ile500 (Table 2). It is possible that these residues comprised an additional intermediate timescale. Ile164 and Ile500 also displayed comparatively large $\Delta\delta_{2,3}$ values of 12 and 14 Hz, respectively. Here again, the correlated variation in k_{ex} and $\Delta\delta$ values suggested that conformational changes of the catalytic core were coupled to that of the plough region.

In state **4** (Figure 2b), the dead-end complex, all conformational dynamics involving Ile96 (Figure 6b), Ile164, Ile258, Ile449 and Ile563 were completely suppressed. Motion could only be detected for Ile488 and Ile500, with the former displaying k_{ex} values characteristic of an intermediate timescale (similar to Ile164 and Ile500 in state **3** above) and the latter similar to that seen for group I residues. Clearly, the dynamic nature of the dead-end complex was different from all other states both in the distribution as well as the magnitudes of the k_{ex} values. It has been suggested that P2 in this dead-end or stalled state can be reinitiated by supplementation with the missing NTPs (38). However, this reinitiated complex has a greatly reduced polymerization rate than that prior to stalling. Interestingly, the polymerization rate in the reinitiated complex had no measurable temperature dependence (in the 16–30°C range) (38) which suggests that the conformational sub-states likely giving rise to the RF-field dependent $\Gamma_{MQ,eff}$ were no longer thermally accessible for this state. This implied that the enzyme was transformed into a distinct conformation that was still capable of catalysis, but no longer efficient in doing so. The distinct conformation adopted by the stalled complex was also evident from $\Delta\delta_{3,4}$values that were, on average, far larger than corresponding values for the other ternary complexes, namely states **5** and **6** ($\Delta\delta_{3,5}$ and $\Delta\delta_{3A,6}$ discussed below, also see Supplementary Figure S4). Another observation unique to state **4** was that the Ile37 resonance showed extensive line broadening seemingly due to an unresolved doublet (Supplementary Figure S5). Based on $\Delta\Gamma_{MQ,eff} = \Gamma_{MQ,eff}\,(31.25\,Hz) - \Gamma_{MQ,eff}\,(1000\,Hz) = 15\,s^{-1}$ (for the major component of the doublet), slow conformational dynamics persisted in this state for Ile37, though the dispersion curve could no longer be reliably fit assuming fast-exchange i. e. using Equation (4).

The distribution of k_{ex} values for the unstable initiation complex (state **5**, see Figure 2b) was as expected, essentially similar to state **3** in their overall distribution—group I (Ile37, Ile96 and Ile500, $k_{ex} = 1411 \pm 149\,s^{-1}$) and group II (Ile164, Ile258, Ile488 and Ile563, $k_{ex} = 453 \pm 91\,s^{-1}$). Ile164 (20 Hz) also displayed a relatively large $\Delta\delta_{3,5}$ value.

Analysis of the motion of states **1–5**, however, did not allow the dissection of the motions that get altered simply by the formation of an initiation complex prior to start of the nucleotide addition cycle i.e. catalysis. In order to do so, data for two additional states (**3A** and **6**), involving the GTP analog GMPCPP, that is non-cleavable between the α and β−phosphates, were analyzed.

While the data for the GMPCPP-bound states was of lower quality than the GMPPNP-bound states, some interesting motional characteristics emerged. For state **3A** (Mg^{2+}/GMPCPP, Table 1), while motional modes and k_{ex} values similar to state **3** were expected, substantial differences were seen (Table 2). This indicated that the nature of perturbations induced by the GTP-analogs GMPPNP and GMPCPP were different, a scenario confirmed by inspection of the $\Delta\delta_{3,3A}$ values (Supplementary Figure S6). Motions involving Ile164, Ile258 and Ile563 were completely suppressed, adding credence to the hypothesis that the motions of these residues were coupled to the conformational fluctuations around the catalytic cavity at the substrate NTP binding sites. Given the fact that the affinities of P2 towards the two GTP analogs were about the same, as mentioned above, it is likely that these differences arose from subtle variations in the orientation of the triphosphate moiety at the active site possibly resulting in altered coupling of the active site to remote regions of the protein. This is discussed at length in the following section.

However, the motional characteristics of Ile37, Ile96 and Ile488 were similar to state **3** (Table 2), though small differences in k_{ex} values for Ile500 with this state was noted. While the k_{ex} value for Ile96 was similar to state **3**, the $\Delta\Gamma_{MQ,eff} = \Gamma_{MQ,eff}\,(31.25\,Hz) - \Gamma_{MQ,eff}\,(1000\,Hz) = 3.8\,s^{-1}$ (compared with $13.2\,s^{-1}$ for state **3**, Figure 6b) most likely due to alteration in $\Delta\omega_H$ or $\Delta\omega_C$ values or both rather than a simple population shift (with respect to state **3**) given that $\Delta\delta_{3,3A}$ value for this residue was quite small.

Finally for state **6** (Figure 2b), the ternary complex of Mg^{2+}/GMPCPP/5′-UUUCC-3′, capable of forming a stable initiation complex was studied. In this state, field-dependent $\Gamma_{MQ,eff}$ could only be detected for Ile37 (characteristic of a group I residue), Ile449 (group II), Ile488 (group II) and Ile500, while no such effects were seen for Ile96, Ile164, Ile258 and Ile563. Thus, the only clear difference between the motional characteristics of the GMPCPP/Mg^{2+} (state **3A**) and the stable initiation complex i.e. the GMPCPP/Mg^{2+}/ssRNA (state **6**) was the suppression of slow dynamics involving Ile96 (template entry) in the latter. This is not unexpected since the ssRNA is now likely locked in a stable complex. Unfortunately the weak signals for the C-terminal Ile617 and Ile641 residues did not allow a quantitative analysis of these resonances. Thus the nature of the motions assigned to facilitate the egress of the daughter strands could not be analyzed. However Ile37 (template entry) was still shown to display a k_{ex} value expected of a group I residue.

CONCLUSIONS

Based on the characterization of the seven states discussed above, the following observations can be made—the slow dynamics in P2 could be generally characterized by two distinct timescales—a faster timescale (group I, k_{ex} ~1200–1500 s^{-1}) and a second, slower timescale (group II, k_{ex} ~500–800 s^{-1}).

The faster timescale (group I) involved residues in close proximity to the template tunnel (Ile37 and Ile96) and on the C-terminal domain. These motions most likely assist in RNA translocation, facilitating the passage of the template through the tunnel and exit of the newly

synthesized daughter strands by coordinated movements of the C-terminal domain. The nature of conformational dynamics in the C-terminal domain was also borne out by the large chemical shift changes in all the complexes with ssRNA—for Ile641, $\Delta\delta_{3,4} = 59$ Hz, $\Delta\delta_{3,5} = 41$ Hz and $\Delta\delta_{3A,6} = 38$ Hz. Given the timescale of these motions, they are clearly not expected to be rate limiting. This is consistent with data obtained for both DNA (44) and RNA polymerases (29) where the translocation is not rate limiting in the process of polymerization. It has been suggested that the translocation step is coupled to pyrophosphate release from the enzyme. Rates of pyrophosphate release in have been found to be as slow as $1200\,s^{-1}$ in T7 DNA polymerase (44) and as fast as $8100\,s^{-1}$ in 3Dpol (29). The k_{ex} values of group I residues were within this range of timescales. Formation of a stable initiation complex lead to suppression of the motion of the fingertip Ile96 (Figure 6b) while that of the Ile37, that is closest to the ssRNA template, remained. This suggests that some motion around the template tunnel is required to thread the ssRNA through the RdRP even after the formation of an initiation complex. Ile96 was also no longer mobile in the stalled complex and motion involving Ile37 occurred on a slower exchange regime.

The second, slower motional mode (group II) that coincides with the catalytic timescale, involved several residues located in the catalytic motifs (motif C—Ile449, motif D—Ile488 and motif E—Ile500) and in the outer edge of the template tunnel (Ile164, Ile258 and Ile563). The distribution of k_{ex} values within these groups of residues suggests that there may be multiple motional modes involved in producing them. This fact is supported by the observation of selective damping of motions at the outer edge of the template tunnel upon binding GMPCPP, a behavior distinct from GMPPNP binding. This also suggests that minor perturbations at the active site can cause activation or deactivation of a subset of these modes involving distant regions of P2. It has been proposed that one of the conformational changes that occur on the catalytic timescale likely involves the reordering of the triphosphate moiety and concurrent changes in the enzyme (29). Given the differences induced by GMPPNP and GMPCPP both in static chemical shifts (in Ile145, Ile164, Ile449 and Ile500) and dynamics changes (in Ile164, Ile258 and Ile563) it is possible that this reorientation contributes in part to one component of the slower timescale. Indeed the largest differences in the binding mode of these two GTP analogs most likely occur due to the orientation of the triphosphate moiety. An analysis of GTP-bound structures of P2 (e.g. 1H10) reveals that the O atom (CH_2 in GMPCPP) between the α and β-phosphates participates in a hydrogen bond with the Arg270 sidechain, additional hydrogen-bonds are also seen for the β- and γ-phosphates (with basic residues—Arg268, Arg270 and His328) defining their orientation. The conserved motif F (268–272) which has evolved to co-ordinate the triphosphate moiety does not contain any Ile residues, so is invisible to the analysis presented here. Another key observation that emerged from these studies was evidence of long-range coupling of the plough region (as reflected by Ile164) with the catalytic core region reinforcing observations from functional analyses (43).

Upon formation of a dead-end complex (state **4**), motions of Ile449 on motif C are completely suppressed while motion of the motif D residue, Ile488 occurs on a distinct, faster timescale. This dead-end complex also seems structurally distinct from all other RNA-bound states. Interestingly, Ile488 displayed $k_{ex} \sim 600\,s^{-1}$ in all states we analyzed, including the dead-end complex, where it had a slightly higher k_{ex} value compared with the other states. An analysis of the available structures of a range of RdRPs indicate that the conformation of motif D is amongst the most variable (12). It has been suggested that this motif D, which bears a basic residue functioning as a general acid, undergoes a conformational change taking it into an optimal position to protonate the product pyrophosphate. Protonation of the pyrophosphate product leads to a large enhancement in the rate of nucleotidyl transfer (12,16). There are several Lys residues (476, 479 and 487) on motif D in ϕ6 P2, which could serve this purpose.

The case of the motif E residue Ile500 was rather curious. It displayed the largest variation in k_{ex} values (from 690 to $1811\,s^{-1}$) over the several states, being slowest (and closest to the catalytic i.e. group II timescale) for states **1**, **3**, **3A** and **6**, and fastest (and closest to a group I timescale) for states **2**, **4** and **5**. The exact reason for this variation is unclear at the present time. Notably, Ile500 also showed significant chemical shift variations across the various states.

Another intriguing feature that was immediately evident was that several residues that were dynamic on the slow, μs–ms timescale (with significant k_{ex} values) across the states analyzed, were also dynamic on the fast, ps–ns timescale (with low η and consequently low S^2_{axis} values). These included Ile37, Ile96 near the template entry portal and Ile488, Ile500 at the substrate entry portal near the catalytic site. It is likely that motion on multiple timescales at the portal regions implies slow sampling of conformational states of the enzyme as well as local conformational variations allowing the processing of a wide range of substrate NTPs and template RNAs, accommodating differences both in overall size and shape as well local structural details.

Clearly, RdRPs in general, and P2 in particular, function as intricate molecular machines with many moving parts working in unison. This study that used 25 probes of molecular mobility represents a first step towards understanding these motions in a more quantitative way. We have only attempted to interpret the k_{ex} values in the present approach. Analysis of the chemical shifts and populations of the two states should also be highly informative (45–48), as would the extension of these studies to other methyl-bearing sidechains including Val, Leu, Met residues and finally to the backbone ^{15}N nuclei. A drawback of our approach and indeed that of others is that we interpret field (ν_1)-independent $\Gamma_{MQ,eff}$ values as lack of μs–ms timescale motion. RF-field-independent $\Gamma_{MQ,eff}$ may also occur if the differences in chemical shifts between the ground and excited states for

^{1}H or ^{13}C nuclei are vanishingly small i.e. $\Delta\omega_H$ or $\Delta\omega_C$ are 0. Thus, it is often useful to combine MQ dispersion measurements with corresponding SQ experiments. This, while easier to carry out in smaller, well-behaved proteins, is a non-trivial task in P2. In spite of these shortcomings, to the best of our knowledge this is the very first attempt to quantify dynamics along the catalytic cycle of this very important class of RNA processing enzymes. Additionally, the only complete kinetic analysis for the nucleotide addition cycle has been performed for the poliovirus RdRP (3Dpol) (29) that uses a primer to drive the nucleotide addition cycle. This is different from RdRPs like P2 that initiate RNA synthesis *de novo*. Thus, while the major dynamic modes contributing to the enzymatic activity may be similar, differences in the spatial as well as temporal features are likely present between the two sub-classes. It would therefore be important to use kinetic assays in *de novo* initiating RdRPs in conjunction with NMR analyses or conversely to extend our NMR experiments to RdRPs such as 3Dpol for which substantial kinetic data exist.

SUPPLEMENTARY DATA

Supplementary Data are available at NAR Online.

ACKNOWLEDGEMENTS

The authors are grateful to Dr. Paul Gottlieb (CCNY) for his generous gift of the pLM687 plasmid. The authors thank Dr Lewis Kay (U of Toronto) and Dr Dmitry Korzhnev (U of Toronto) for the NMR pulse sequences for relaxation measurements and Dr Aneel Aggarwal (Mt. Sinai School of Medicine) for use of the Panvera Beacon 2000 spectrofluorimeter. The authors also thank Dr Andrea Piserchio (CCNY/NYSBC), Dr Leonard Mindich (PHRI), Dr Stewart Shuman (Sloan-Kettering Institute) and Dr Fabien Ferrage (CNRS, Ecole Normale Supérieure, Paris) for critical comments on this manuscript.

FUNDING

National Science Foundation MCB0843141 (RG); National Institues of Health 5G12 RR03060 (partial support of the core facilities at CCNY); National Institutes of Health P41 GM66354 (partial support of NMR facilities at NYSBC). Funding for open access charge: NSF MCB0843141.

Conflict of interest statement. None declared.

REFERENCES

1. Ferrer-Orta,C., Arias,A., Escarmis,C. and Verdaguer,N. (2006) A comparison of viral RNA-dependent RNA polymerases. *Curr. Opin. Struct. Biol.*, **16**, 27–34.
2. Bruenn,J.A. (2003) A structural and primary sequence comparison of the viral RNA-dependent RNA polymerases. *Nucleic Acids Res.*, **31**, 1821–1829.
3. Bruenn,J.A. (1993) A closely related group of RNA-dependent RNA polymerases from double-stranded RNA viruses. *Nucleic Acids Res.*, **21**, 5667–5669.
4. Makeyev,E.V. and Grimes,J.M. (2004) RNA-dependent RNA polymerases of dsRNA bacteriophages. *Virus Res.*, **101**, 45–55.
5. Makeyev,E.V. and Bamford,D.H. (2000) Replicase activity of purified recombinant protein P2 of double-stranded RNA bacteriophage ϕ6. *EMBO J.*, **19**, 124–133.
6. Makeyev,E.V. and Bamford,D.H. (2000) The polymerase subunit of a dsRNA virus plays a central role in the regulation of viral RNA metabolism. *EMBO J.*, **19**, 6275–6284.
7. Mindich,L. (2004) Packaging, replication and recombination of the segmented genome of bacteriophage ϕ6 and its relatives. *Virus Res.*, **101**, 83–92.
8. Poranen,M.M. and Tuma,R. (2004) Self-assembly of double-stranded RNA bacteriophages. *Virus Res.*, **101**, 93–100.
9. Butcher,S.J., Grimes,J.M., Makeyev,E.V., Bamford,D.H. and Stuart,D.I. (2001) A mechanism for initiating RNA-dependent RNA polymerization. *Nature*, **410**, 235–240.
10. Salgado,P.S., Makeyev,E.V., Butcher,S.J., Bamford,D.H., Stuart,D.I. and Grimes,J.M. (2004) The structural basis for RNA specificity and Ca^{2+} inhibition of an RNA-dependent RNA polymerase. *Structure*, **12**, 307–316.
11. Poranen,M.M., Salgado,P.S., Koivunen,M.R., Wright,S., Bamford,D.H., Stuart,D.I. and Grimes,J.M. (2008) Structural explanation for the role of Mn^{2+} in the activity of ϕ6 RNA-dependent RNA polymerase. *Nucleic Acids Res.*, **36**, 6633–6644.
12. Cameron,C.E., Moustafa,I.M. and Arnold,J.J. (2009) Dynamics: the missing link between structure and function of the viral RNA-dependent RNA polymerase? *Curr. Opin. Struct. Biol.*, **19**, 1–7.
13. Steitz,T.A. (1999) DNA polymerases: structural diversity and common mechanisms. *J. Biol. Chem.*, **274**, 17395–17398.
14. Ranjith-Kumar,C.T. and Kao,C.C. (2006) Recombinant viral RdRps can initiate RNA synthesis from circular templates. *RNA*, **12**, 303–312.
15. Biswal,B.K., Cherney,M.M., Wang,M., Chan,L., Yannopoulos,C.G., Bilimoria,D., Nicolas,O., Bedard,J. and James,M.N. (2005) Crystal structures of the RNA-dependent RNA polymerase genotype 2a of hepatitis C virus reveal two conformations and suggest mechanisms of inhibition by non-nucleoside inhibitors. *J. Biol. Chem.*, **280**, 18202–18210.
16. Castro,C., Smidansky,E.D., Arnold,J.J., Maksimchuk,K.R., Moustafa,I., Uchida,A., Gotte,M., Konigsberg,W. and Cameron,C.E. (2009) Nucleic acid polymerases use a general acid for nucleotidyl transfer. *Nature Struct. Mol. Biol.*, **16**, 212–218.
17. Arnold,J.J., Vignuzzi,M., Stone,J.K., Andino,R. and Cameron,C.E. (2005) Remote site control of an active site fidelity checkpoint in a viral RNA-dependent RNA polymerase. *J. Biol. Chem.*, **280**, 25706–25716.
18. Bressanelli,S., Tomei,L., Rey,F.A. and De Francesco,R. (2002) Structural analysis of the hepatitis C virus RNA polymerase in complex with ribonucleotides. *J. Virol.*, **76**, 3482–3492.
19. Di Marco,S., Volpari,C., Tomei,L., Altamura,S., Harper,S., Narjes,F., Koch,U., Rowley,M., De Francesco,R., Migliaccio,G. *et al.* (2005) Interdomain communication in hepatitis C virus polymerase abolished by small molecule inhibitors bound to a novel allosteric site. *J. Biol. Chem.*, **280**, 29765–29770.
20. Palmer,A.G. 3rd. (2001) NMR probes of molecular dynamics: overview and comparison with other techniques. *Annu. Rev. Biophys. Biomol. Struct.*, **30**, 129–155.
21. Wolf-Watz,M., Thai,V., Henzler-Wildman,K., Hadjipavlou,G., Eisenmesser,E.Z. and Kern,D. (2004) Linkage between dynamics and catalysis in a thermophilic-mesophilic enzyme pair. *Nature Struct. Mol. Biol.*, **11**, 945–949.
22. Eisenmesser,E.Z., Millet,O., Labeikovsky,W., Korzhnev,D.M., Wolf-Watz,M., Bosco,D.A., Skalicky,J.J., Kay,L.E. and Kern,D. (2005) Intrinsic dynamics of an enzyme underlies catalysis. *Nature*, **438**, 117–121.
23. Tzakos,A.G., Grace,C.R., Lukavsky,P.J. and Riek,R. (2006) NMR techniques for very large proteins and RNAs in solution. *Annu. Rev. Biophys. Biomol. Struct.*, **35**, 319–342.

24. Tugarinov,V. and Kay,L.E. (2005) Methyl groups as probes of structure and dynamics in NMR studies of high-molecular-weight proteins. *ChemBioChem*, **6**, 1567–1577.
25. Goger,M., McDonnell,J.M. and Cowburn,D. (2003) Optimization of protein assignment with reduced cycle multidimensional NMR experiments. *Spectroscopy*, **17**, 161–167.
26. Korzhnev,D.M., Kloiber,K. and Kay,L.E. (2004) Multiple-quantum relaxation dispersion NMR spectroscopy probing millisecond time-scale dynamics in proteins: theory and application. *J. Am. Chem. Soc.*, **126**, 7320–7329.
27. Tugarinov,V. and Kay,L.E. (2006) Relaxation rates of degenerate 1H transitions in methyl groups of proteins as reporters of side-chain dynamics. *J. Am. Chem. Soc.*, **128**, 7299–7308.
28. Tugarinov,V., Sprangers,R. and Kay,L.E. (2007) Probing side-chain dynamics in the proteasome by relaxation violated coherence transfer NMR spectroscopy. *J. Am. Chem. Soc.*, **129**, 1743–1750.
29. Arnold,J.J. and Cameron,C.E. (2004) Poliovirus RNA-dependent RNA polymerase (3Dpol): pre-steady-state kinetic analysis of ribonucleotide incorporation in the presence of Mg^{2+}. *Biochemistry*, **43**, 5126–5137.
30. Mindich,L., Qiao,X., Onodera,S., Gottlieb,P. and Frilander,M. (1994) RNA structural requirements for stability and minus-strand synthesis in the dsRNA bacteriophage ϕ6. *Virology*, **202**, 258–263.
31. Boggs,P.T., Donaldson,J.R., Byrd,R.H. and Schnabel,R.B. (1989) ODRPACK software for weighted orthogonal distance regression. *ACM Trans. Math. Software*, **15**, 348–364.
32. Tugarinov,V., Ollerenshaw,J.E. and Kay,L.E. (2005) Probing side-chain dynamics in high molecular weight proteins by deuterium NMR spin relaxation: an application to an 82-kDa enzyme. *J. Am. Chem. Soc.*, **127**, 8214–8225.
33. Korzhnev,D.M., Kloiber,K., Kanelis,V., Tugarinov,V. and Kay,L.E. (2004) Probing slow dynamics in high molecular weight proteins by methyl-TROSY NMR spectroscopy: application to a 723-residue enzyme. *J. Am. Chem. Soc.*, **126**, 3964–3973.
34. Dittmer,J. and Bodenhausen,G. (2004) Evidence for slow motion in proteins by multiple refocusing of heteronuclear nitrogen/proton multiple quantum coherences in NMR. *J. Am. Chem. Soc.*, **126**, 1314–1315.
35. Garcia de la Torre,J., Huertas,M.L. and Carrasco,B. (2000) HYDRONMR: prediction of NMR relaxation of globular proteins from atomic-level structures and hydrodynamic calculations. *J. Magn. Reson.*, **147**, 138–146.
36. van Dijk,A.A., Makeyev,E.V. and Bamford,D.H. (2004) Initiation of viral RNA-dependent RNA polymerization. *J. Gen. Virol.*, **85**, 1077–1093.
37. Kainov,D.E., Lisal,J., Bamford,D.H. and Tuma,R. (2004) Packaging motor from double-stranded RNA bacteriophage ϕ12 acts as an obligatory passive conduit during transcription. *Nucleic Acids Res.*, **32**, 3515–3521.
38. Vilfan,I.D., Candelli,A., Hage,S., Aalto,A.P., Poranen,M.M., Bamford,D.H. and Dekker,N.H. (2008) Reinitiated viral RNA-dependent RNA polymerase resumes replication at a reduced rate. *Nucleic Acids Res.*, **36**, 7059–7067.
39. Nygren,J., Svanvik,N. and Kubista,M. (1998) The interactions between the fluorescent dye thiazole orange and DNA. *Biopolymers*, **46**, 39–51.
40. Arias,A., Arnold,J.J., Sierra,M., Smidansky,E.D., Domingo,E. and Cameron,C.E. (2008) Determinants of RNA-dependent RNA polymerase (in)fidelity revealed by kinetic analysis of the polymerase encoded by a foot-and-mouth disease virus mutant with reduced sensitivity to ribavirin. *J. Virol.*, **82**, 12346–12355.
41. Wang,C. and Palmer,A.G. 3rd. (2002) Differential multiple quantum relaxation caused by chemical exchange outside the fast exchange limit. *J. Biomol. NMR*, **24**, 263–268.
42. Laurila,M.R., Salgado,P.S., Stuart,D.I., Grimes,J.M. and Bamford,D.H. (2005) Back-priming mode of ϕ6 RNA-dependent RNA polymerase. *J. Gen. Virol.*, **86**, 521–526.
43. Sarin,L.P., Poranen,M.M., Lehti,N.M., Ravantti,J.J., Koivunen,M.R., Aalto,A.P., van Dijk,A.A., Stuart,D.I., Grimes,J.M. and Bamford,D.H. (2009) Insights into the pre-initiation events of bacteriophage ϕ6 RNA-dependent RNA polymerase: towards the assembly of a productive binary complex. *Nucleic Acids Res.*, **37**, 1182–1192.
44. Patel,S.S., Wong,I. and Johnson,K.A. (1991) Pre-steady-state kinetic analysis of processive DNA replication including complete characterization of an exonuclease-deficient mutant. *Biochemistry*, **30**, 511–525.
45. Hansen,D.F., Vallurupalli,P. and Kay,L.E. (2009) Measurement of methyl group motional parameters of invisible, excited protein states by NMR spectroscopy. *J. Am. Chem. Soc.*, **131**, 12745–12754.
46. Vallurupalli,P., Hansen,D.F. and Kay,L.E. (2008) Structures of invisible, excited protein states by relaxation dispersion NMR spectroscopy. *Proc. Natl Acad. Sci. USA*, **105**, 11766–11771.
47. Vallurupalli,P., Hansen,D.F. and Kay,L.E. (2008) Probing structure in invisible protein states with anisotropic NMR chemical shifts. *J. Am. Chem. Soc.*, **130**, 2734–2735.
48. Hansen,D.F., Vallurupalli,P., Lundstrom,P., Neudecker,P. and Kay,L.E. (2008) Probing chemical shifts of invisible states of proteins with relaxation dispersion NMR spectroscopy: how well can we do? *J. Am. Chem. Soc.*, **130**, 2667–2675.